Magnetic Relaxation in the Solar Corona

Kenneth Miller[1], Bengt Fornberg[2], Natasha Flyer[3], & B. C. Low[4]

May 1, 2008

ABSTRACT

This is a mathematical study of the long-lived hydromagnetic structures produced in the tenuous solar corona by the turbulent, resistive relaxation of a magnetic field under the condition of extremely high electrical conductivity. The relaxation theory of Taylor (1974), originally developed for a laboratory device, is extended to treat the open atmosphere where the relaxing field must interact with its surrounding fields. A boundary-value problem is posed for a two dimensional model that idealizes the corona as the half Cartesian plane filled with a potential field (i) that is anchored to a rigid, perfectly conducting base, and, (ii) that embeds a force-free magnetic field in the form of a flux rope oriented horizontally and perpendicular to the Cartesian plane. The flux rope has a free boundary which is an unknown in the construction of a solution for this atmosphere. Pairs of magnetostatic solutions are constructed to represent the initial and final states of a flux-rope relaxation that conserves both the total magnetic helicity and total axial magnetic flux, using a numerical iterative method specially developed for this study. The collection of numerical solutions found provides an insight into the interplay among several hydromagnetic properties in the formation of long-lived coronal structures. In particular, the study shows (i) that the outward spread of reconnection between a relaxing flux-rope and its external field may be arrested at some outer magnetic flux-surface within which a constant-α force-free field emerges as the minimum-energy state, and, (ii) that this outward spread is complicated by an inward, partial collapse of the relaxing flux-rope produced by a loss of internal magnetic pressure.

Subject headings: MHD — Sun: magnetic fields — Sun: corona

[1]Department of Mathematics and Statistics, Wichita State University

[2]Department of Applied Mathematics, University of Colorado

[3]Institute for Mathematics Applied to the Geosciences, National Center for Atmospheric Research

[4]High Altitude Observatory, National Center for Atmospheric Research

1. Introduction

Force-free magnetic fields are physically the simplest form of the long-lived hydromagnetic structures populating the tenuous corona of the Sun (Aschwanden 2005; Low 1996). Fully ionized at its million-degree temperature, the corona under quiescent conditions may be taken to be a perfect electrical conductor. Neglecting pressure and gravity as a first approximation, a coronal equilibrium structure is one whose electric current density is everywhere parallel to the magnetic field $\mathbf{B}$ expressed by

$$\nabla \times \mathbf{B} = \alpha \mathbf{B}, \tag{1}$$
$$\nabla \cdot \mathbf{B} = 0. \tag{2}$$

The proportionality function α in equation (1) describes twist in the magnetic field. Applying the solenoidal condition (2) to this equation gives

$$\mathbf{B} \cdot \nabla \alpha = 0, \tag{3}$$

showing that α takes a constant value along each line of force. This paper is concerned with the turbulent, resistive relaxation of magnetic fields that produces long-lived coronal structures described by these generally nonlinear equations (Aly 1989; Sakurai 1989; Low & Lou 1992; Flyer et al. 2004; Hu & Wang 2005; Wolfson 2003; Wolfson et al. 2007; Low & Flyer 2007).

In the presence of an ubiquitous magnetic field of 10 G or greater, the characteristic Alfven speed in the tenuous corona is of the order of 10^3 km/s. The transit time of an Alfven wave crossing a coronal structure of a typical length of 10^5 km is about 100 s. When a hydromagnetic structure becomes ideally unstable, the instability has a rise time of the order of that transit time. The different parts of the structure must exchange information at typically the Alfven speed to bring about a growing perturbation. An instability may either saturate or run away with a significant release of energy, such as in a flare, depending on the amount of energy stored in the unstable structure. In the case of a flare, the runaway release of energy is dissipative in spite of the high coronal electrical conductivity. Spontaneous current sheets form in the manner described by Parker (1994) to rapidly heat the plasma to tens of millions of degrees in temperature. A host of plasma kinetic processes then sets in to couple nonlinearly and nonlocally with the fluid behaviors of the corona (Alexander & Metcalf 2003; Aschwanden 2005; Krucker & Lin 2003; Lin et al. 2003; Magara et al. 1996; Shibata et al. 1995; Shibata 1999; Tsuneta 1996a; Tsuneta 1996b).

Flares often occur when fresh magnetic flux emerges into the corona from the photosphere below (Lites et al. 1995, Lites 2005, Okamoto et al. 2007, Shibata et al. 1990,

Manchester 2001, Manchester et al. 2004, Fan 2001, Fan & Gibson 2004, Amari 2003, Magara 2006). Hereafter we qualify the terms field and flux to be magnetic only when confusion would otherwise arise. The intermixing of fresh and pre-existing fluxes produces flares which have the principal effect of removing excess energy to bring about a combined flux system in a quiescent low-energy state (Manchester et al. 2004, Amari 2004, Zhang & Low 2003). The energy of this system may build up during a slow quasi-static evolution, as photospheric motions of the order of 1 km/s twist and shear the magnetic field. The slow evolution has a time scale of days, extremely long compared to the Alfven transit time in the corona, leading to further flaring whenever circumstances are encountered that favor additional shedding of excess energy (Aly & Amari 2007, Forbes & Priest 1995, Gibson et al. 2002, Titov & Demoulin 1999, Low & Berger 2003).

These considerations suggest the following properties for a long-lived structure in static equilibrium. It must be stable to both infinitesmal and finite perturbations in order to build up the large amount of free energy that eventually gets liberated in a flare. By the Parker theory, spontaneously forming current-sheets are a ready means of dissipating the stored energy. Therefore, the build up of stored energy must also rely on some hydromagnetic constraints that prevent spontaneous current-sheets from draining away all the stored energy. In this concern, the theory of Taylor (1974, 1986) is physically especially pertinent. This theory is based on the idea that, as current sheets dissipate under conditions of high conductivity, the dissipation of magnetic-helicity has a time scale much longer than that of magnetic energy liberation (Berger 1984). Magnetic helicity is a topological measure of twist in the magnetic field. It is twist that gives the force-free field its field-aligned current as a stored energy. Therefore, the approximate conservation of magnetic helicity prevents a field from losing that twist, or, equivalently, from relaxing to a current-free or potential state. The relevance of magnetic helicity to the solar atmosphere was first pointed out by Heyvaerts & Priest (1984) and has since gain much recognition (Amari, Luciani & Aly 2000, Demoulin 2007, Demoulin et al. 2006, Low 1996, Zhang & Low 2005, Zhang 2006). Even as current sheets form spontaneously and dissipate during a non-explosive evolution, this conservation law limits the amount of energy liberated by this process. This conservation law also applies in the case of a significant energy liberation during a flare. In other words, if the flaring structure has a net twist as represented by a significant net helicity, the flare must still leave behind in the field an energy associated with that approximately unchanged total helicity. Only by removing this total helicity can the field finally attain its potential state with its absolutely minimum energy; see the mechanism relating to coronal mass ejections described in Zhang & Low (2005).

We present a two-dimensional model for comparing the energies and structural properties of the initial and final states in a Taylor-like relaxation. We extend this theory originally

developed for a magnetic field wholly contained in a laboratory device to treat the interaction of the relaxing field with an external field in an open atmosphere (Dixon et al 1989, Janse & Low 2007). In Sections 2 and 3, we construct, analytically and numerically, families of pairs of initial-final states that are used in Section 4 to illustrate the basic physics of magnetic relaxation in the corona. We conclude with a summary of our results in Section 5.

2. The Free Boundary Problem

An actual turbulent relaxation interupting a quasi-static evolution of a coronal magnetic field is an extremely complex phenomenon. It involves a host of plasma and hydromagnetic processes taking place with the full three-dimensional freedom of physical space. The details of these time-dependent processes may be regarded not to be essential in the simplifying view that all they do is to dump excess magnetic energy in order to enable the field to recover a metastable equilibrium state. From that state, quasi-static evolution takes over again. Avoiding full-blown numerical time-dependent hydromagnetic simulations of the turbulent relaxation is not so limiting at this stage of development. Those simulations may be helped in the future by the insight offered by our simple approach of examining possible pairs of intial-final equilibrium states linked by applicable hydromagnetic conservation laws. The construction of such equilibrium-pairs is formulated below.

Consider a magnetic field that varies with Cartesian coordinates x and y but is independent of z:

$$\mathbf{B} = \left(\frac{\partial A}{\partial y}, -\frac{\partial A}{\partial x}, Q \right), \tag{4}$$

expressed in its solenoidal form in terms of a flux function A and the component Q in the direction of the ignorable coordinate. Then, the force-free equations (1) and (3) require $Q(x, y) = Q(A)$ so that for a known form of $Q(A)$, A satisfies the elliptic partial differential equation

$$\nabla^2 A + Q(A)Q'(A) = 0. \tag{5}$$

In this derivation, $\alpha = Q'(A)$ so that a uniform Q corresponds to the potential field. Let us use the solutions to this equation to describe magnetic structures in the half-space $y > 0$ idealized to be the solar corona. For a given form of $Q(A)$, we need to solve a boundary value problem for A subject to (i) a given distribution of B_y at the atmospheric base $y = 0$, and, (ii) the demand for $\mathbf{B}$ to vanish at infinity in $y > 0$.

We are interested in solutions describing a straight rope of twisted magnetic field that is oriented horizontally in the z direction. This rope is spatially confined in the $x - y$ plane but blends continuously into a potential field in the unbounded exterior of the rope.

Except for the two special cases:

$$Q = \alpha_0 \left(A - A_0 \right), \tag{6}$$

$$\nabla^2 A + \alpha_0^2 \left(A - A_0 \right) = 0, \tag{7}$$

and,

$$Q = \lambda \sqrt{2} \left(A - A_0 \right)^{1/2}, \tag{8}$$

$$\nabla^2 A + \lambda^2 = 0, \tag{9}$$

where α_0, A_0, and λ are constants, equation (5) is formidably nonlinear. Equation (6) describes a force-free field with a constant $\alpha = \alpha_0$. In contrast, equation (8) describes a force-free field with a variable

$$\alpha = \frac{\lambda}{\sqrt{2}} \left(A - A_0 \right)^{-1/2}. \tag{10}$$

Although this class of fields are nonlinear, the governing equations in this case are reduced to the linear equation (9) for A. By Ampere's law, the electric current density is

$$\nabla \times \mathbf{B} = \left(\frac{\partial Q}{\partial y}, -\frac{\partial Q}{\partial x}, -\nabla^2 A \right), \tag{11}$$

except for a constant multiplier. Equation (9) shows that the fields it generates have a uniform current density in the z direction. Henceforth, we refer to the fields generated by equations (7) and (9) as the constant-α and uniform axial-current fields. Both classes of fields, if taken to fill all space in $y > 0$, have unacceptable physical properties, but they will be rendered useful in the model we now formulate.

2.1. Twisted Flux Rope with a Free Boundary

Our model requires a continuous field that has a spatially variable-α inside the rope of twisted field but with a negligible α in the exterior of the rope. We avoid this formidable nonlinear boundary value problem by adopting an alternative approach. Let the rope make a cross section σ with the $x - y$ plane, denoting its boundary by $\partial \sigma$. Set $Q \equiv 0$ in the exterior, denoted by σ', where the field $\mathbf{B} = \mathbf{B}_{pot}$ is purely potential:

$$\mathbf{B}_{pot} = \left(\frac{\partial A_{pot}}{\partial y}, -\frac{\partial A_{pot}}{\partial x}, 0 \right), \tag{12}$$

$$\nabla^2 A_{pot} = 0. \tag{13}$$

Then, to complete the model, we only have to prescribe $Q(A) \neq 0$ in σ for the twisted field in the flux rope. Admitting a general force-free field in σ would bring us back to nonlinear

boundary value problems we are avoiding. Therefore, to keep the mathematical problem simple, we demand for the field in σ to be a solution of either equations (7) or (9), taking advantage of their linearity.

This formulation yields a free-boundary problem, with $\partial\sigma$ as an unknown to be constructed self-consistently with the flux function A governed by the respective partial differential equations in σ and σ'. A more complicated free-boundary problem is encountered in the model of Low & Berger (2003) that embeds a twisted flux-rope in an external field that is also twisted. In contrast, we are considering a simpler model, the case of a twisted flux-rope embedded in an external untwisted field. In both instances, we have avoided the mathematical challenge of treating equation (5) as a nonlinear partial differential equation, only to encounter it in the form of a free-boundary problem that also defies a general treatment. The numerical methods developed for the free-boundary problem formulated in this paper are a first step to similar methods to deal with the more challenging problems of Low & Berger.

For the field given by equation (4), the flux function A is constant along a line of force, from which follows that $\alpha = Q'(A)$ is constant along a line of force. There can be no connection between the lines of force in σ, where $\alpha \neq 0$, and those in σ', where $\alpha = 0$. Therefore $\partial\sigma$ is a curve in the $x - y$ plane along which A takes a constant value A_0. We assume that $\partial\sigma$ is a regular curve. In other words, the flux-rope boundary $\partial\sigma$ is a magnetic flux surface on which $A = A_0$. The governing equations for A show that upon crossing $\partial\sigma$, say, from σ into σ', the solution A may have, at worst, discontinuous derivatives of second or higher orders. It then follows that the solutions of A are assured of continuity of its first partial derivatives across $\partial\sigma$, which, in turn implies that $\mathbf{B}$ is continuous everywhere.

We limit our attention to the case of $\partial\sigma$ being a simple closed curve lying entirely in $y > 0$. Therefore, the flux function A_{pot} accounts for the normal flux distribution on $y = 0$ and must meet the requirement that the field vanishes at infinity in $y > 0$. We consider the specific case of $\mathbf{B}_{pot}$ satisfying

$$B_y|_{y=0} = B_0 \frac{x}{1 + x^2}, \tag{14}$$

which is equivalent to specifying

$$A|_{y=0} = -\frac{1}{2} B_0 \log\left(x^2 + 1\right). \tag{15}$$

This boundary condition describes a bipolar flux distribution at the base of the atmosphere identified with $y = 0$. In addition, we also require in $y > 0$,

$$as \quad (x^2 + y^2)^{1/2} \to \infty, \quad |\nabla A| \to 0. \tag{16}$$

Our free boundary problem seeks a solution A of the respective equations in σ and σ' subject to: (i) A taking a constant value on $\partial\sigma$, (ii) A being continuous across $\partial\sigma$, and, (iii) $A = A_{pot}$ in σ' satisfying boundary conditions (15) and (16).

2.2.   Analytical Solutions

In order to avoid wordy sentences, we henceforth refer to a magnetic field $\mathbf{B}$ in terms of its flux function A, keeping in mind that $\mathbf{B}$ may involve a non-zero $B_z = Q$. The potential field A_{pot} should be distinguished from the field A_{min}

$$A_{min} = -\frac{1}{2}B_0 \log\left(x^2 + (y+1)^2\right),\tag{17}$$

that is *everywhere* potential in $y > 0$ with $Q = 0$, meeting that same boundary conditions (15) and (16). This is the minimum-energy state of all fields satisfying these boundary conditions. The potential field A_{pot} may be viewed to be the modification from A_{min} as the result of a magnetic flux rope occupying the region σ in $y > 0$. The precise form of A_{pot} depends on the shape of $\partial\sigma$ and the current in σ.

For the specific boundary conditions (15) and (16), analytical global solutions can be constructed such that both A_{pot} and the force-free field in σ are all cylindrically symmetric about the point $(x, y) = (0, 1)$. This is the motivation for using boundary condition (15) but a word of clarification concerning magnetic energy is in order for this case. Although the potential fields $\mathbf{B}_{pot}$ and $\mathbf{B}_{min}$ vanish at infinity as required under boundary condition (16), they have unbounded total magnetic energies in $y > 0$. This is an artifact of the two-dimensional unbounded space adopted for our model. The unboundedness of energy is due to an infinitely-long, straight, virtual line-current in $y < 0$ implied by boundary condition (15). The force-free, i.e., non-potential, fields in $y > 0$, subject to boundary conditions (15) and (16), all also have unbounded energies but each of them has a finite energy difference ΔE satisfying

$$\infty > \Delta E = \int_{y>0} \left(\mathbf{B}^2 - \mathbf{B}_{min}^2\right) dxdy > 0,\tag{18}$$

thus retaining the idea of $\mathbf{B}_{min}$ being a minimum-energy state.

Introduce the cylindrical polar coordinates centered at $(x, y) = (0, 1)$:

$$x = R\cos\varphi,\tag{19}$$
$$y - 1 = R\sin\varphi,\tag{20}$$

in terms of which the field (4) has the representation:

$$\mathbf{B} = \frac{1}{R}\frac{\partial A}{\partial \varphi}\hat{R} - \frac{\partial A}{\partial R}\hat{\varphi} + Q\hat{z}. \tag{21}$$

Identify $\partial\sigma$ with $R = R_1$, a circle of constant radius, defining the regions $\sigma : R < R_1$ and $\sigma' : R > R_1$. For cylindrically symmetric fields with no variation in φ, $B_R = 0$. Equation (7) can be integrated as an ordinary differential equation to give

$$Q^2 = 2\int_R^{R_1} \frac{dA}{dR}\frac{1}{R}\frac{d}{dR}\left[R\frac{dA}{dR}\right]dR, \tag{22}$$

which can be rewritten as

$$B_z^2 = 2\int_R^{R_1} B_\varphi \frac{1}{R}\frac{d}{dR}\left[RB_\varphi\right]dR. \tag{23}$$

Entire families of force-free fields in σ can be generated by prescribing $B_\varphi(R)$ for B_z to be determined by equation (23), subject to the condition that the integral on its right hand side is positive definite. The choice of the integration constant in the above derivation ensures that $B_z = 0$ at $R = R_1$ where B_φ and A must match the potential field

$$\mathbf{B}_{pot} = \frac{B_0}{R}\hat{\varphi}, \tag{24}$$

$$A_{pot} = -B_0\log R. \tag{25}$$

in the external region σ' in accordance with boundary condition (15). The global field is then everywhere continuous. We now proceed to construct the twisted flux rope in σ.

2.2.1. The Constant-α Flux Rope

Inside σ place the force-free field generated by the solution of equation (7):

$$\mathbf{B} = \frac{B_0}{R_1 J_1(\alpha_0 R_1)}\left[J_1(\alpha_0 R)\hat{\varphi} + J_0(\alpha_0 R)\hat{z}\right], \tag{26}$$

$$A = \frac{B_0}{R_1\alpha_0 J_1(\alpha_0 R_1)}J_0(\alpha_0 R) - B_0\log R_1, \tag{27}$$

where J_0 and J_1 are Bessel functions, and we assume that α_0 takes a constant value for a given R_1 such that

$$J_0(\alpha_0 R_1) = 0. \tag{28}$$

This ensures the continuity of B_z across the boundary $\partial\sigma$, taking note that $B_z = Q = 0$ everywhere in σ'. In this solution we have also set $A_0 = -B_0\log R_1$ in equation (7) for the

continuity of A across $\partial\sigma$. Then, A is everywhere continuous up to its first derivatives and $\mathbf{B}$ is continuous with $\mathbf{B}_{pot}$ across $\partial\sigma$.

The total axial flux of the flux rope is

$$
\begin{aligned}
F_0 &= \int_\sigma B_z dxdy, \\
&= \frac{2\pi B_0}{\xi_1} R_1,
\end{aligned}
\tag{29}
$$

writing $\xi_1 = \alpha_0 R_1$, and the total relative magnetic helicity of the flux rope is

$$
\begin{aligned}
H_R &= \int_\sigma AQ dxdy, \\
&= \frac{\pi B_0^2}{\xi_1} \left(1 - 2\log R_1\right) R_1,
\end{aligned}
\tag{30}
$$

using the formula of Zhang, Flyer & Low (2006). These quantities will be of physical interest later in the development.

The solutions we have constructed form a family parametrized by the single parameter R_1 which by definition is less than unity. The parameter B_0 is held fixed so that all these solutions satisfy the same boundary condition (15). The solid curve in Figure 1 displays H_R as a function of F_0 over the range $R_1 < 1$.

2.2.2. Uniform Axial-Current Flux Rope

As the second example, place a cylindrically symmetric force-free field into σ that satisfies equation (9). Direct construction gives inside σ:

$$
\mathbf{B} = \frac{B_0}{R_1^2} R\hat{\varphi} + \frac{\sqrt{2}B_0}{R_1^2} \left(R_1^2 - R^2\right)^{1/2} \hat{z},
\tag{31}
$$

$$
A = \frac{B_0}{2R_1^2} \left(R_1^2 - R^2\right) - B_0 \log R_1,
\tag{32}
$$

where we have set $\lambda^2 = \frac{2B_0}{R_1^2}$. This magnetic field matches across the boundary $\partial\sigma$ continuously into the potential field $\mathbf{B}_{pot}$ given by equations (24) and (25). As in the previous example, the global A is everywhere continuous up to its first derivatives.

The total axial flux of the flux rope is

$$
F_0 = \frac{2}{3}\sqrt{2}\pi B_0 R_1,
\tag{33}
$$

and the total relative magnetic helicity of the flux rope is

$$H_R = \frac{1}{15}\sqrt{2}\pi B_0^2 R_1 \left(3 - 10\log R_1\right). \tag{34}$$

These quantities will be of physical interest later in the development. Again we have a one-parameter family of solutions generated by R_1 holding B_0 fixed. The solid curve in Figure 2 displays H_R as a function of F_0 in the range $R_1 < 1$.

2.2.3. A High-Energy Flux Rope

We provide a third example of a cylindrically symmetric flux rope:

$$B_\varphi = B_1\sqrt{R}\sin kR, \tag{35}$$

$$B_z = B_1\left[2(R_1 - R) + \frac{1}{2k}\sin 2kR + R\cos^2 kR\right]^{1/2}, \tag{36}$$

for the force-free field in σ, where k is an arbitrary positive constant and $B_1 = \frac{B_0}{R^{3/2}}$ to ensure that this field is continuous with the potential field in σ'. From its definition, the flux function $A(R)$ in σ can be determined from B_φ by a single integration, with a choice of the integration constant to ensure continuity of the flux function across $R = R_1$. Then the total axial flux F_0 and total helicity H_R can be computed. No analytical formula is available for these quantities. For fixed F_0 and H_R, the energy contained in the flux rope depends on the specific distribution of the field. This third example contains considerably more energy in the flux rope than the two previous examples with the same F_0 and H_R, a point useful later in our development.

3. Numerical Solutions

The cylindrically symmetric solutions are useful illustrations of flux ropes with free boundaries. In the physical theory to be discussed in the next section, a flux rope in this model is characterized with F_0 and H_R as independent, invariant physical parameters. Hence, we need to generate flux-rope solutions with at least 2 free parameters, that is, the assumption of a circular shape for $\partial\sigma$ is too restrictive.
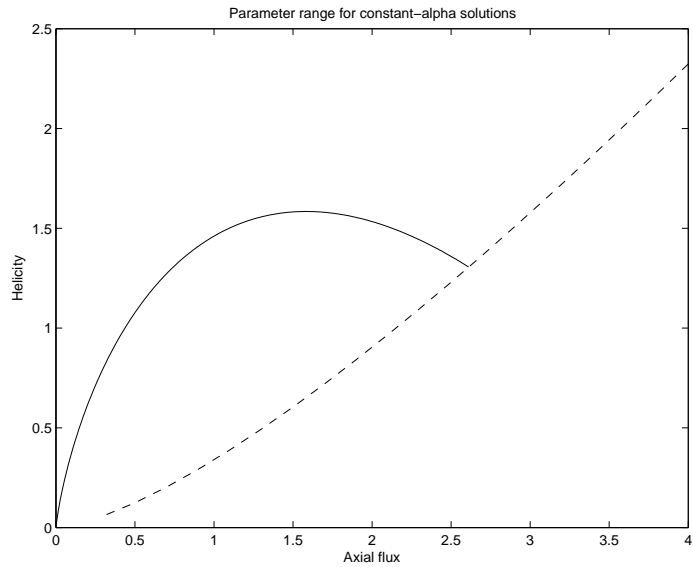
Fig. 1.— The solid curve shows the values of F_0 and H_R for which there is an analytic constant-α field with $B_0 = 1$. For all parameter pairs (F_0, H_R) above the dashed curve there is a solution to the constant-α free boundary problem with the flux rope cross-section contained entirely in the upper half plane $y > 0$ (for those pairs on the dashed curve the flux rope boundary is tangent to $y = 0$). For parameters off the solid curve these solutions are found numerically.
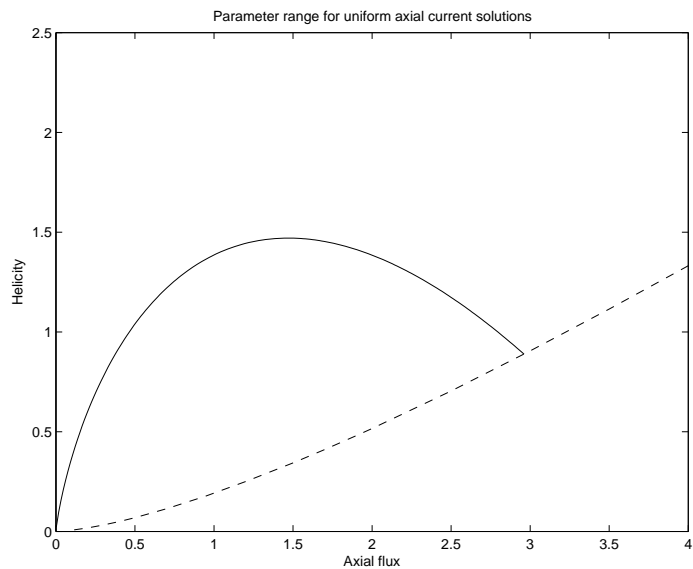

Fig. 2.— The same as Figure 1 except for uniform axial current fields. The total parameter domain is larger and the solid curve strictly lower than in Figure 1.

3.1. The Numerical Method

We assume that the above free-boundary value problem is well-posed. To solve it, a modification of the numerical method employed in Elcrat et al. (2000, 2001) for the study of steady inviscid fluid flows with vorticity is used. Our task is given prescribed values for the axial flux F_0 and total relative magnetic helicity H_R as defined in (29) and (30), find the solution $A(x, y)$ in (5) together with the domain σ, boundary value A_0, and constant λ (uniform axial-current) or α_0 (constant α) such that the prescribed values of F_0 and H_R are realized. The explanation of the procedure is divided into two parts: (1) the transformations necessary to map the upper-half plane to a smooth finite domain and (2) the iterative procedure that is used to calculate the solution.

3.1.1. Mappings

Figure 3 shows that to go from the physical (x, y) plane to the computational (ξ, η) plane requires 3 mappings, the first and second being conformal and the third not. Our goal is to map the upper half plane to a square, so as to be able to nicely grid it. In the first step, the upper half of the physical x, y-plane is interpreted as the upper half of the complex plane. We use a bilinear mapping to map it to the inside of a circle centered at the origin in the new w-plane. This origin, back in the physical plane, corresponds to a point on the imaginary axis we shall call a (we shall later see the role a plays). In the opposite direction, the origin in the physical (x, y)-plane now corresponds to 1. Next, in step 2, we map the inside of the circle to the semi-infinite strip with 1 being mapped back to the origin but the origin being mapped to infinity. Lastly, in step 3, the semi-infinite strip is mapped to the square $[0, 1]\mathrm{x}[0, 1]$.

In Figure 4, we see that by performing the reverse mappings, the grid of the computational plane represent circles nested about the point a in the physical plane. The reason is that a lattice of horizontal and vertical lines in the computational (ξ, η)-plane will have the same features in the u-plane and thus be straight radii from the origin and concentric circles around the origin in the w-plane. By a well-known property of bilinear mappings, the curves in the physical z-plane must then be circles (or straight lines, in the case they extend to infinity).

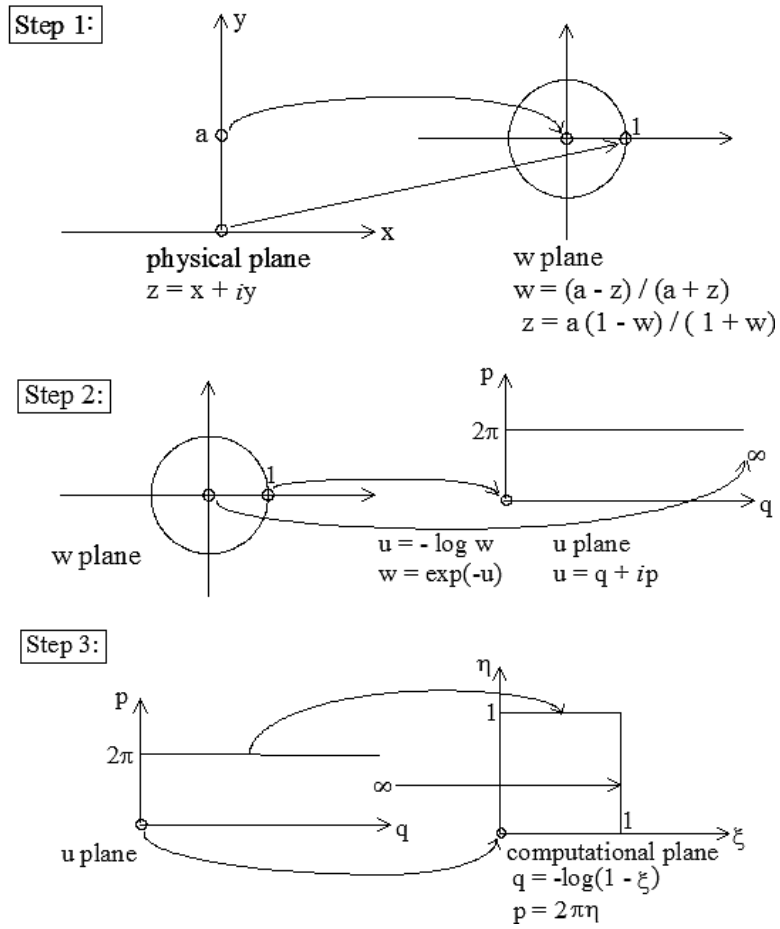After these mappings the partial differential equation (PDE) for the uniform axial cur-

Fig. 3.— The mappings required to map the upper half plane to the square $[0,1] \times [0,1]$.
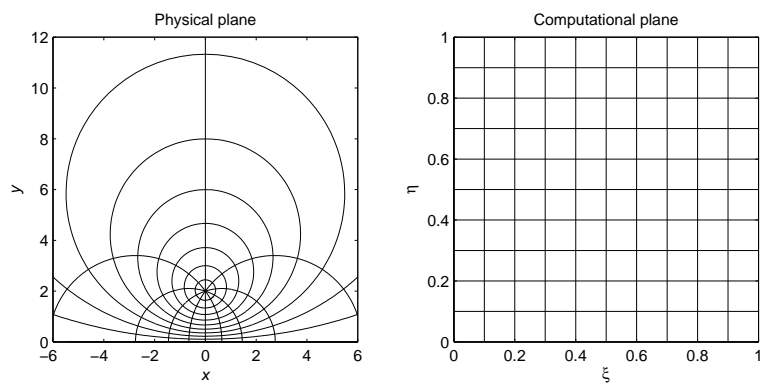

Fig. 4.— The computational domain displayed back in the physical plane.

rent field, (9), in terms of the ξ and η becomes

$$(1 - \xi)^2 \frac{\partial^2 A}{\partial \xi^2} - (1 - \xi)\frac{\partial A}{\partial \xi} + \frac{1}{4\pi^2}\frac{\partial^2 A}{\partial \eta^2} = \tag{37}$$

$$- \lambda^2 |a|^2 (cos(2\pi\eta) + \frac{(1 - \xi)^2 + 1}{2(1 - \xi)})^{-2}.$$

By subtracting the minimum energy potential flux function A_{min}, (17), from A in (37) the resulting unknown function will satisfy a zero boundary condition at $\xi = 0$ ($\xi = 0$ in the computational square corresponds to the x-axis in the physical domain). Since there is periodicity in the η direction for $0 \leq \xi \leq 1$, it is natural to turn to the Fourier space in the η variable. We therefore take the Fast Fourier Transform in η of the right hand side of (37) and solve the resulting transformed ordinary differential equation in ξ using centered second order finite differences. An accurate boundary condition at $\xi = 1$ is that the zeroth Fourier mode of the solution is the same at the last two grid lines, but that all the other modes vanish at $\xi = 1$. This procedure is non-iterative and provides a very efficient method for solving (37).

All computations are done in terms of the (ξ, η) variables. After A is determined using the Fast Poisson Solver just outlined, the integrals required to determine F_0 and H_R are computed using the trapezoid rule over $0 \leq \xi \leq 1$, $0 \leq \eta \leq 1$.

3.1.2. Iterative procedure

Again, let us consider the uniform axial current field, (9), as an example for describing the iterative method used to solve the nonlinear free-boundary problem (for simplicity we describe it terms of x, y coordinates):

$$\nabla^2 A = \begin{cases} -\lambda^2, & (x, y) \in \sigma \\ 0, & (x, y) \notin \sigma \end{cases}.$$

where A satisfies (15) and (16) and $\sigma = \{(x, y) : A > A_0, \ y > 0\}$. By boundary condition (15), $A < 0$ on $y = 0$, suggesting that if σ does not intersect that boundary, $A_0 > 0$ and $A > A_0$ inside σ as we have assumed. The constants λ and A_0, as well as the region σ, are unknown and are to be determined so that F_0 and H_R assume given prescribed values. During the nth iterative step, for given λ_n and A_{0n}, they are computed numerically

$$F_0 = \iint Q\, dx\, dy = \sqrt{2}\, \lambda_n \iint_{A_n > A_{0n}} (A_n - A_{0n})^{1/2}\, dx\, dy$$

and

$$H_R = \iint AQ \, dx \, dy = \sqrt{2} \, \lambda_n \iint_{A_n > A_{0n}} A_n (A_n - A_{0n})^{1/2} \, dx \, dy.$$

The steps are as follows:

1. Make an initial guess for λ, σ, and A_0. Set iteration number to $n = 1$.

2. Call the MATLAB routine *fsolve* which is a nonlinear equation solver. This routine will vary λ and A_0 until the prescribed values of F_0 and H_R are reached within a given tolerance by repeatedly solving the discretized PDE and evaluating the integrals for F_0 and H_R over the area $A > A_0$ via the trapezoidal rule. The fast Poisson solver for (37) solves (9) quickly and accurately. Generally, *fsolve* will need to solve the PDE 10 to 15 times.

3. Even though F_0 and H_R will have converged to the desired values, there will be a discrepancy between the area defined by $A > A_0$ and the area σ since A_0 was varied and σ was kept fixed throughout step 2. The area σ is redefined to be the domain where $A > A_0$, the iteration number is increased by one, and we go back to step 2 with this new σ.

4. Steps 2 and 3 are repeated until the set of grid points in σ_n and σ_{n-1} are identical. This generally requires anywhere from 10 to more than 50 calls to *fsolve*.

Only a slight modification of this algorithm is needed to solve the free-boundary problem for a constant-α field:

$$\nabla^2 A = \begin{cases} -\alpha_0^2 (A - A_0), & (x, y) \in \sigma \\ 0, & (x, y) \notin \sigma. \end{cases}$$

For this problem we iteratively solve the linear equation

$$\nabla^2 A_n = \begin{cases} -\alpha_n^2 (A_{n-1} - A_{0n}), & (x, y) \in \sigma_{n-1} \\ 0, & (x, y) \notin \sigma_{n-1}. \end{cases} \tag{38}$$

where $\sigma_n = \{(x, y) : A_n > A_{0n}, \ y > 0\}$ for $n \geq 1$. Again the values of α_n and A_{0n} are varied in an inner iterative routine until F_0 and H_R assume prescribed values to within a certain tolerance, where now

$$F_0 = \alpha_n \iint_{A_n > A_{0n}} (A_n - A_{0n}) \, dx \, dy$$

$$H_R = \alpha_n \iint_{A_n > A_{0n}} A_n (A_n - A_{0n}) \, dx \, dy.$$

The outer iterations are continued until

$$||(A_n - A_{0n})\chi_{\sigma_n} - (A_{n-1} - A_{0,n-1})\chi_{\sigma_{n-1}}|| < \epsilon$$

for some tolerance ϵ (the value 10^{-5} is generally used), where $||f||$ denotes the maximum of $|f(\xi, \eta)|$ over the unit square and $\chi_\sigma(\xi, \eta) = 1$ for values of (ξ, η) corresponding to points $(x, y) \in \sigma$, but is otherwise zero. Note that by using the previous A_{n-1} on the right hand side of (38) rather than adding the term $\alpha_n^2 A_n$ to the left hand side of the differential equation, we are able to use the same Fast Poisson Solver for this problem as before.

The exact cylindrical solutions provide a means for testing the accuracy of the numerical method. The constant-α solution with $R_1 = 0.8$ and $B_0 = 1$ will provide a specific test case. For an $N \times N$ grid, the numerical methods used to compute the flux and helicity are accurate with an absolute error of about 6×10^{-5} for $N = 300$ and 2×10^{-5} for $N = 500$. Since $F_0 = 2.0902$ and $H_R = 1.5115$ in this case, relative accuracy is comparable. To check the accuracy of the Fast Poisson Solver, the equation

$$\nabla^2 A = -\alpha_0^2 (A_e - A_{e0})\chi$$

can be solved, where A_e is the exact solution (27) and χ is the characteristic function of the set $\{A_e - A_{e0} > 0\}$. The error $||A - A_e||$ is 2×10^{-4} for $N = 300$ and 2×10^{-5} for $N = 500$. To test the complete algorithm, taking the characteristic function of the circle centered at $1.1i$ and of radius 1 as an initial guess, and using the values of flux and helicity for the cylindrical solution with $R_1 = .8$ as the prescribed flux and helicity parameters, the full numerical procedure can be run. With $N = 300$ it converges to a numerical solution A satisfying $||A - A_e|| = 2.5 \times 10^{-4}$.

3.2. Representative Numerical Solutions

In all the numerical solutions described below B_0 is taken to be one. Figure 5 shows representative surface plots of the computed flux functions A for both a uniform axial current field and a constant-α field. Numerical solutions to the constant-α problem can be found for all choices of F_0 and H_R above the dashed curve in Figure 1. Similarly the dashed curve in Figure 2 indicates the boundary of the parameter domain in the uniform axial current case. Any solution for parameters above the dashed curve has $A_0 > 0$ and hence the boundary $\partial\sigma$ of the cross-section of the corresponding flux rope is entirely in the upper half-plane $y > 0$. The parameter domain boundary is obtained by a modification of the general algorithm described above: A_0 is set to zero and only F_0 is prescribed, with only λ varying in the inner iterations and H_R determined after the completion of the iterative process.
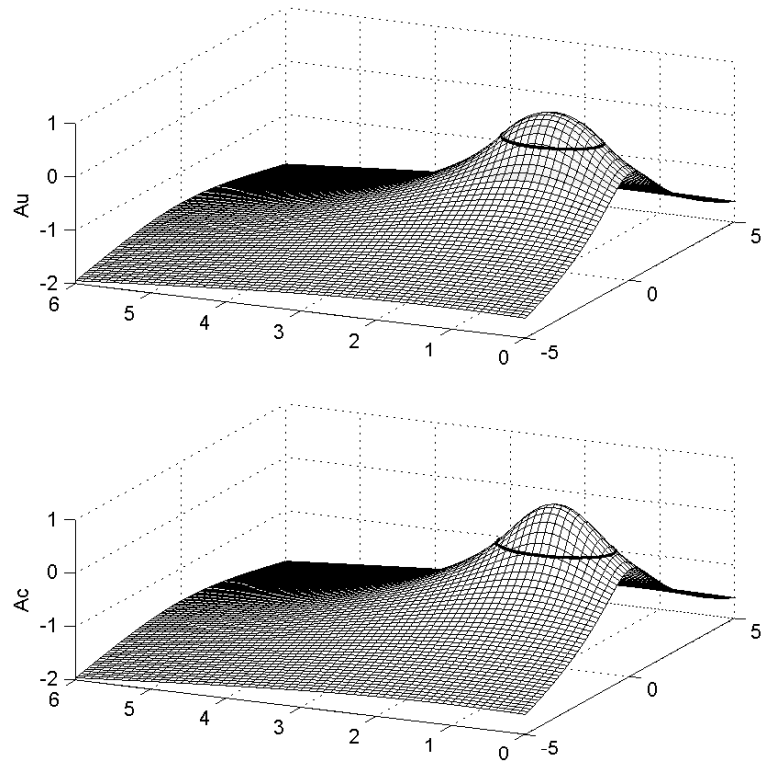
Fig. 5.— Surface plots for A_u, the uniform axial current field flux function, and for A_c, the constant-α flux function, for $F_0 = 2$, $H_R = 1.5$.

We have found only one solution to each free-boundary problem for any given admissible parameter pair, despite attempts to find multiple solutions by using different initial guesses for the iterative method.

Let $(0, y_u)$ and $(0, y_c)$ denote the centroids of the cross-sections for the computed uniform axial current and constant-α flux ropes respectively. For fixed F_0 and H_R, we find that $y_c < y_u$. Also both y_c and y_u are increasing as functions of H_R when F_0 is held fixed. The solid curves in Figures 1 and 2 show the parameters for which there are analytic solutions as described in Section 2.2 and for these parameters the flux ropes have circular cross section centered at $y = 1$ on the y-axis. For both the constant-α and the uniform axial current solutions, the computed flux rope cross-sections are very nearly circular except when A_0 is close to 0, i.e. except when the flux and helicity parameters are close to the parameter domain boundaries shown in Figures 1 and 2. The examples given in Figures 6 and 7 show that for A_0 close to 0 the cross-sections are distinctly non-circular. For parameters below the solid curve the cross sections are wider in the x direction, while for those above the solid curve the cross sections are wider in the y direction.

3.3. Energy Computation

Formally the magnetic field (4) has total energy

$$\iint_{y>0} (|\nabla A|^2 + Q(A)^2)\, dx\, dy,$$

however this integral is infinite. To avoid this divergence we consider the energy difference relative to the minimum energy potential state A_{min}, (17). We denote by E this energy
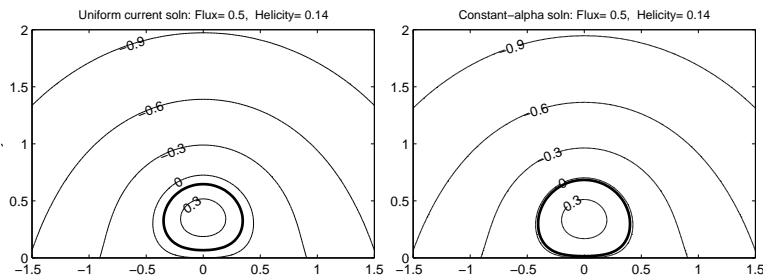

Fig. 6.— Contour plots for both the uniform axial current solution A_u and the constant-α solution A_c for $F_0 = 0.5$, $H_R = 0.14$. The thicker contour indicates the flux tube boundary. The values of A_u and A_c on the flux tube boundaries are $A_{u0} = 0.123$ and $A_{c0} = 0.025$.

difference,

$$E = \iint_{y>0} (|\nabla A|^2 - |\nabla A_{min}|^2 + Q(A)^2) \, dx \, dy \,.$$

Using the identities

$$|\nabla A|^2 = \nabla \cdot (A \nabla A) - A \nabla^2 A \quad \text{and} \quad |\nabla A_{min}^2| = \nabla \cdot (A_{min} \nabla A_{min}),$$

the two-dimensional Gauss theorem and (5), we obtain

$$E = -\int_{y=0} A(\frac{\partial A}{\partial y} - \frac{\partial A_{min}}{\partial y}) dx + \iint_\sigma (AQ(A)Q'(A) + Q(A)^2) \, dx \, dy \,. \tag{39}$$

For the uniform axial current case, $AQ(A)Q'(A) = \lambda^2 A$ and $Q(A)^2 = \lambda^2 2(A - A_0)$ on σ and 0 elsewhere. For the constant-α case, $AQ(A)Q'(A) + Q(A)^2 = 2\alpha_0 QA - \alpha_0 A_0 Q$. This leads to the following formulas for the energy difference for the constant-α and uniform axial current cases:

$$E_c = I + \alpha_0(2H_R - A_0 F_0) \tag{40}$$

$$E_u = I + \iint_\sigma \lambda^2(3A - 2A_0) \, dx \, dy \tag{41}$$

where I is the line integral

$$I = -\int_{y=0} A \frac{\partial(A - A_{min})}{\partial y} dx. \tag{42}$$

Numerically, the double integral in (41) can be computed by using the trapezoid rule, after transforming to an integral over the computational square, with accuracy comparable
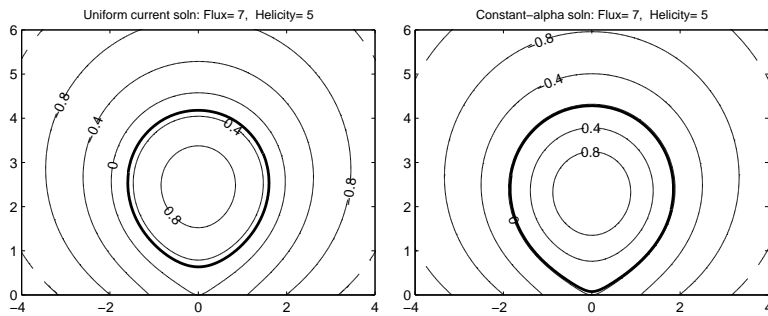

Fig. 7.— Contour plots for $F_0 = 7$, $H_R = 5$. The values of A_u and A_c on the tube boundaries are $A_{u0} = 0.291$ and $A_{c0} = 0.021$.

to that noted above for the computation of F_0 and H_R. Transforming I to an integral in terms of the computational variables gives

$$I = -2\pi \int_0^1 A \frac{\partial v}{\partial \xi}\Big|_{\xi=0} d\eta.$$

However, because this integral is improper with a singularity at $(\xi, \eta) = (0, .5)$ (corresponding to the point at infinity in the physical domain), the accuracy in applying the trapezoid rule directly to this integral is found to be 1 to 2 orders of magnitude worse than the accuracy noted above for the other numerical methods being applied. By making use of the particular nature of the singularity, a method for evaluating the integral with improved accuracy can be found as follows. First note that since $A = A_{min}$ on $y = 0$, by symmetry (42) can be written

$$I = \int_0^M log(x^2 + 1) \frac{\partial v}{\partial y} dx + \int_M^\infty \frac{log(x^2 + 1)}{x^2} (x^2 \frac{\partial v}{\partial y}) dx,$$

with $v = A - A_{min}$. The first of these two integrals will be approximated by the trapezoid rule; we give an estimate for the second.

$$\int_M^\infty \frac{log(x^2 + 1)}{x^2} dx \le 2\frac{(log(M) + 1)}{M} + \frac{1}{3}M^{-3}$$

and

$$\lim_{x \to \infty} x^2 \frac{\partial v}{\partial y} = \lim_{\eta \to \frac{1}{2}}(-ia)\frac{sin^2(2\pi\eta)}{(1 + cos\, 2\pi\eta)}\frac{\partial v}{\partial \xi} = -i2a \lim_{\eta \to \frac{1}{2}}\frac{\partial v}{\partial \xi} = L$$

where a is the point on the imaginary axis used in defining the transformation to computational variables. The limiting value of $\partial v/\partial \xi$ can be computed by a finite difference approximation at the grid point nearest $1/2$. We can take M large enough that M^{-3} is numerically insignificant by letting c be a grid point on the η axis slightly larger than $\frac{1}{2}$, with M the image of c under the coordinate transformation. We obtain

$$I \simeq -4\pi \int_c^1 A_0 \frac{\partial(A - A_{min})}{\partial \xi}\Big|_{\xi=0} d\eta + 2L\frac{(log(M) + 1)}{M}. \tag{43}$$

Again the exact cylindrical constant-α solution with $R_1 = 0.8$ can be used for testing the accuracy of the numerical method. The value of I for the exact cylindrical solution is $I = 2\pi B_0^2 log\, 2$, so by (40)-(42), $E_c = 2\pi B_0^2(1 + log\, 2 - log\, R_1)$. For $R_1 = 0.8$ and $B_0 = 1$ this yields $E_c = 12.04041$. The numerical method gives this value with an error of 1.1×10^{-4} for $N = 300$ and 3×10^{-5} for $N = 500$.

For somewhat larger values of the parameters F_0 and H_R the accuracy of the energy computations is somewhat worse than the preceding error estimate indicates. Some idea

of the accuracy can be obtained by considering the variation in the computed values of the energy when, for given F_0 and H_R, different choices are made of the initial guesses σ_0 and λ_1 and the parameter a. For example with the values $F_0 = 3.5$, $H_R = 3$ and $N = 300$, computed values of the energy vary in the intervals $17.6352 < E_c < 17.6380$ and $17.8486 < E_u < 17.8530$. This indicates a relative accuracy of about 2×10^{-4}. However, because the values of E_u and E_c are quite close, there is significant loss of precision in computing the energy drop $\Delta E = E_u - E_c$. For this example ΔE varies over the range $.2106 < \Delta E < .2178$, so ΔE is accurate to only two significant figures, and the accuracy in the computation of the relative energy drop $\Delta E / E$ is comparable. By increasing the number of grid points to $N = 800$, which is done for some of calculations reported in the next section, the accuracy in computing the relative energy drop is improved to almost 3 significant figures.

3.4. Energy Comparison

For any choice of F_0 and H_R in the parameter domain indicated in Figure 1, the value of E_c, the energy of the computed constant-α solution with axial flux F_0 and relative magnetic helicity H_R, is less than the value of E_u, the energy of the computed uniform axial current solution with the same flux and helicity. The first column of Figure 8 shows the computed energy values E_u and E_c for three different one parameter cross-sections of the parameter domain: in the first case the axial flux is held fixed, $F_0 = 1$; in the second case helicity is fixed, $H_R = 1.8$; in the third case parameters are restricted so that $A_{c0} = .25$, where A_{c0} is the value on the boundary $\partial \sigma$ for the constant-α solution A_c. Each plot in the first column of Figure 8 actually contains plots of both E_u and E_c, but the values are so close that it is difficult to distinguish between them. The second column plots the energy drop $\Delta E = E_u - E_c$ using a different vertical scale. The third column shows the relative energy drop $\Delta E / E_c$ as a percentage.

Several observations can be made on the basis of these numerical comparisons.

1) The (absolute) energy drop appears to be roughly linear as a function of H for fixed F_0, at least for the range of values shown in the Figure 8. The rate of change $\Delta(\Delta E)/\Delta H$ decreases as F_0 increases: the rate being about .071 for $F_0 = 1$ and .047 for $F_0 = 2$.

2) The maximum energy drop is about 1.5%. The maximum relative energy drop occurs when $A_{c0} = 0$, i.e. when the boundary $\partial \sigma$ of the constant-α flux rope touches the x-axis. The relative energy drop increases as either H_R or F_0 approaches the boundary of the parameter domain.
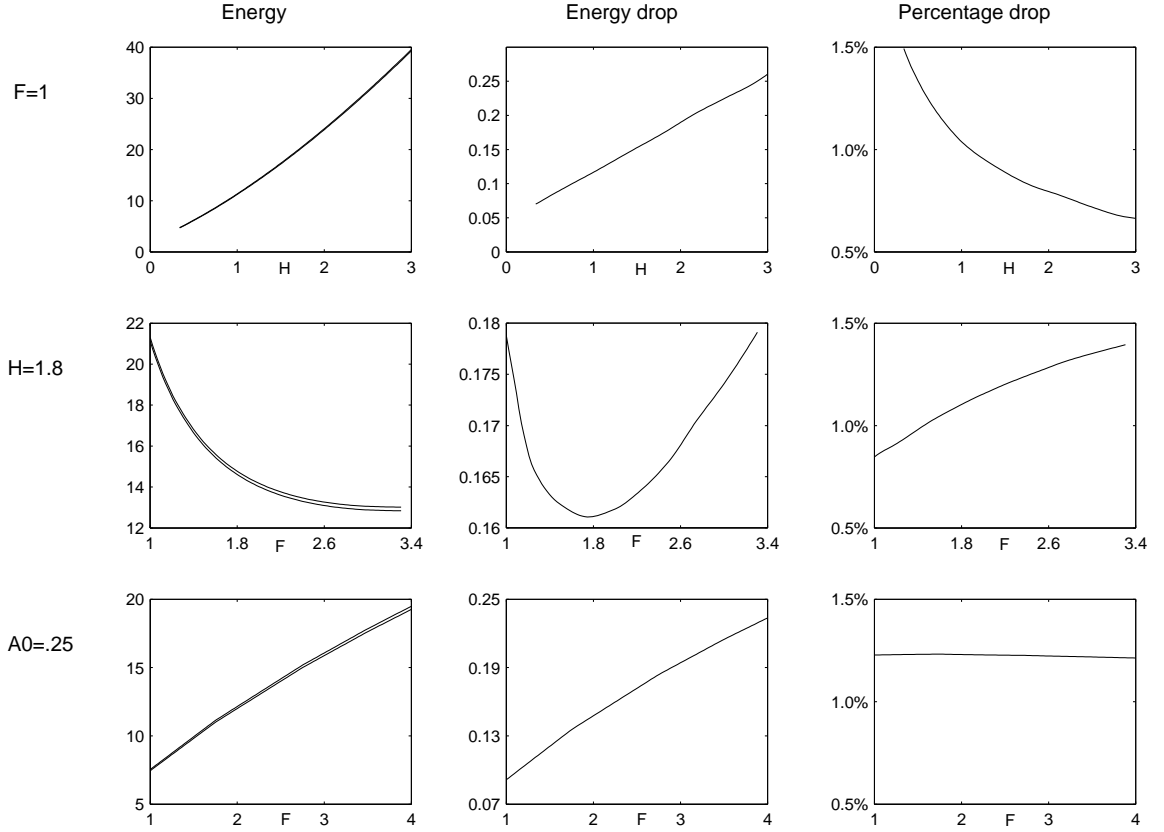
Fig. 8.— Comparison of the energy E_u of uniform axial current fields with the energy E_c of constant-α fields with the same flux and helicity. Three different cross-sections of the parameter domain are considered: a) with flux fixed, $F_0 = 1$; b) with helicity fixed, $H_R = 1.8$; and c) with A_{c0} fixed, $A_{c0} = .25$. In each case plots are shown of the energy (both E_u and E_c), the energy drop $\Delta E = E_u - E_c$ and the relative energy drop $\Delta E/E_c$.

3) The relative energy drop is nearly constant for fixed A_{c0}. For $A_{c0} = .25$, the example shown in the last row of Figure 8, the relative energy drop varies over the range $.0121 < \Delta E/E_c < .0123$, essentially the same as the variation in answers for a single parameter choice, as discussed at the end of the preceding section. The percentage energy drop is about 0.9% for all cases with $A_{c0} = 1$, 1.0% for $A_{c0} = .75$, and 1.1% for $A_{c0} = .5$. For $A_{c0} = 0$, i.e. on the boundary of the parameter domain, the energy drop varies between 1.38% and 1.52%, a greater variation than for a single parameter pair, with the relative energy drop decreasing while moving out along the parameter boundary curve.
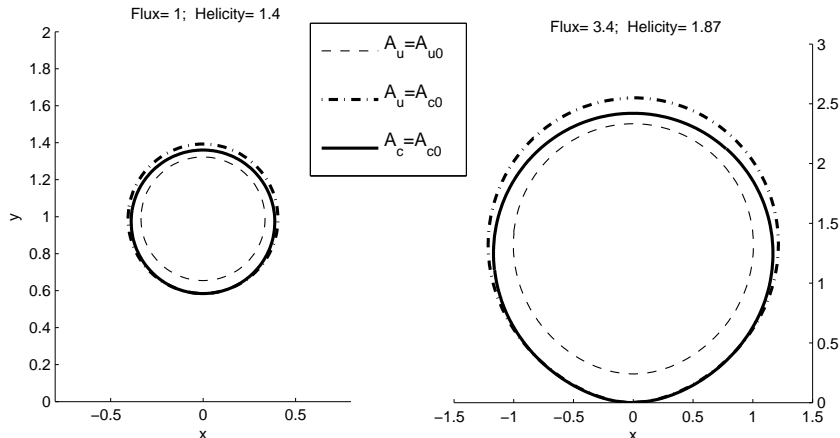

Fig. 9.— In both examples the thin dashed curve is the flux rope boundary for the initial, higher energy state and the solid curve is the flux rope boundary in the relaxed state. The region inside $A = A_{c0}$ implodes as a result of the energy release. There is little or no contraction at the point closest to the x-axis. Similar behavior is observed in all the computed cases.

4.   Magnetic-Field Relaxation in the Solar Corona

Our numerical free-boundary solutions are direct illustrations of some general hydro-magnetic concepts used to understand long-lived coronal structures. The comparison of the initial and final states of a relaxation, linked by the relevant conservation laws, has been typically indirect or incomplete in the papers published in this area of work. This is because the nonlinear force-free equations are formidable, even when adopting the simplifying two-dimensional models treated in this paper.

In this section, we interpret the physics implied by the free-boundary solutions. The physical properties are described in a unified manner, grouped under several concerns and

beginning with the extension of the Taylor theory.

4.1.   The Original Taylor Theory

The original theory of Taylor (1974) was formulated for a hydromagnetic plasma confined in a perfectly conducting, rigid container. This theory considers the turbulent transition from a given unstable state to a lower-energy state under the assumption of a tenuous but extremely high conducting plasma so that the end state is a force-free field. The relaxation proceeds via spontaneous formation of current sheets that dissipate resistively despite the high conductivity (Parker 1994). The magnetic reconnection produced by current-sheet dissipation changes the field topology (3; Yamada 2001). This change liberates the magnetic energy that sustains the turbulent flows and heats the plasma resistively. Let us first recall the specifics of the original Taylor theory as a step to its extension to the open atmosphere.

For a magnetic field $\mathbf{B}$ wholly contained in a simply connected domain V with boundary wall S, we have the boundary condition

$$B_n = 0 \ on \ S, \tag{44}$$

where n denotes the outward normal direction at S. The solenoidal condition (2) allows us to express

$$\mathbf{B} = \nabla \times \mathbf{A}, \tag{45}$$

in terms of the vector potential $\mathbf{A}$; we will relate this vector to the flux function A later in the development. The magnetic helicity density is given by

$$h = \mathbf{A} \cdot \mathbf{B}, \tag{46}$$

that integrates to give the total helicity

$$H_T = \int_V \mathbf{A} \cdot \mathbf{B} dV. \tag{47}$$

The helicity density h given by equation (46) is dependent on the free gauge of $\mathbf{A}$ (Jackson 1965). But, the total helicity H_T is independent of that gauge by virtue of boundary condition (44). This gauge independence renders H_T a physically meaningful quantity and as a topological measure of magnetic twist.

The evolution of the magnetic field is given by the equation

$$\frac{\partial \mathbf{B}}{\partial t} = \nabla \times (\mathbf{v} \times \mathbf{B} - \eta \nabla \times \mathbf{B}), \tag{48}$$

describing Faraday induction due to the plasma velocity $\mathbf{v}$ and the diffusion of magnetic field with a coefficient of resistivity η taken to be a constant here for simplicity. The diffusion time for a field of scale L is of the order of $\tau_D = L^2/\eta$. Taking the corona to be a fully ionized Hydrogen plasma at its million degree temperature, the conductivity based on the formula of Spitzer (1965) implies a very small resistivity η such that fields of scales of the order of $L \approx 1\ km$ have diffusion time scales of months, quite irrelevant to time scales of about $10^3\ s$ characteristic of energy release in a flare. Hence, the resistive term in equation (48) is negligible except at locations where thin current-sheets are found.

If η is rigorously zero, the total helicity H_T is conserved. Resistive dissipation, i.e., $\eta \neq 0$, destroys magnetic energy and magnetic helicity, an irreversible process. But, under the high conductivity conditions in the corona, resistive dissipation occurs only in the localized regions of transient current sheets. The actual resistive heating of a single event of current-sheet dissipation may not be large, whereas the change in field topology can make available magnetic energy that drives plasma flows that is otherwise locked under the conditions of perfect conductivity. The released energy can then be converted into heat by dynamical processes. For example, in the classical Petchek reconnection process, the plasma is heated principally not at the small reconnection sites but by the slow hydromagnetic shocks in the reconnection-generated flow (Kulsrud 1998).

On the other hand, outside of the thin layers of resistive dissipation, the flow is approximately ideal and field topology as measured by magnetic helicity is conserved. This is the intuitive basis for the Taylor (1974) theory to postulate that the time scale of resistive dissipation of the total helicity H_T is irrelevantly long compared to that of magnetic energy release, under conditions of high conductivity. This postulate can be demonstrated in terms of an inequality between the two time scales (Berger 1984).

For a magnetic field dominated plasma, the end-state of a turbulent relaxation is one containing a force-free field. Then, taking the total helicity H_T to be conserved, the Taylor theory identifies that force-free field to have the absolute minimum of all the energies of all the fields sharing that conserved total helicity H_T. By the theorem of Woltjer (1958), this field satisfies equations (1) and (2) with a constant $\alpha = \alpha_0$, subject to (i) boundary condition (44), and, (ii) the determination of α_0 to endow the field with the total helicity H_T. The spatial uniformity of α expresses a spreading of the magnetic twist throughout the magnetic field.

4.2. Taylor Relaxation in an Open Atmosphere

Applying the Taylor theory to an atmosphere presents two complications (Low 1996). In the corona, $\mathbf{B}$ threads across the boundary, the base $y = 0$ in our two-dimensional model where $B_n \neq 0$, and the gauge independence of H_T fails. This is remedied by the use of relative helicity H_R, formulated to be gauge-independent, in place of the total helicity H_T (Berger & Field 1984); see the instructive calculations of Berger (1985). Our model employs the total relative helicity H_R, using a formula derived by Zhang, Flyer & Low (2006); see equations (30) and (34). Hereafter, we simply call H_R the total helicity for brevity.

The second complication comes from the unboundedness of an atmosphere; see the discussion in Low (1996). Spreading a conserved, finite quantity H_R throughout an unbounded domain V produces a diminishingly small density of it. Thus, the Taylor end state for V would, in that limit of vanishingly small helicity density, be no different from the potential field with no local twist. Such a relaxation would, in principle, take infinite time to establish because the far reaches of the atmosphere must acquire twist spread out there by induced magnetic reconnection. Therefore, the Taylor relaxation needs to be modified from this straightforward interpretation in order to apply it to the entire atmosphere .

Start with some initial state containing a twisted flux rope embedded in an external untwisted potential field. A Taylor-like relaxation may set in, as the rope field reconnects within itself and with the untwisted external field to spread magnetic twist outward. This process may proceed until a point is reached when there is no energy available to fuel further reconnection under the applicable hydromagnetic constraint. Although the reconfigured flux rope has eaten into the original external field, the reconnection has stopped at some finite flux surface outside of which the rest of the field remains untwisted. The conserved total helicity is the constraint that relates the initial and final states.

4.3. The Approximate Conservation of the Total Axial Flux

For our two-dimensional model, the invariance of the total axial flux F_0 is an additional conservation law which we now justify under the following physical consideration. During a rapid Taylor relaxation, the dense base $y = 0$ may be approximated to be rigid and perfectly conducting. The resistive term with coefficient η is negligible in equation (48) except at locations where current sheets have formed and are dissipating. In the flux-rope relaxation we are considering, these sheets form in the immediate neighborhood of the rope, leading to reconnection between the twisted fields of the rope and the external untwisted fields in that neighborhood. Let us assume that this growing reconnecting region does not grow to

include the the boundary $y = 0$. Then the electric field near that boundary is given by

$$\mathbf{E} = -\frac{1}{c}\mathbf{v} \times \mathbf{B} \tag{49}$$

neglecting resistive dissipation. Impose from Maxwell's equations that the tangential electric field must always be continuous across a surface. Then noting that the "rigid" region $y < 0$ has zero electric field, under the assumption of perfect conductivity, and that $B_n \neq 0$ in our model, we obtain the boundary condition

$$\mathbf{v} = 0 \; at \; y = 0, \tag{50}$$

as derived by Roberts (1967).

Integrate equation (48) for the rate of change of the total flux in z direction across an area S_1 bounded by a closed curve C_1 in the $x - y$ plane in our model,

$$\frac{d}{dt}\int_{S_1} B_z dx dy = \oint_{C_1} (\mathbf{v} \times \mathbf{B} - \eta \nabla \times \mathbf{B}) \cdot d\mathbf{s}, \tag{51}$$

with an application of Stokes theorem and introducing $d\mathbf{s}$ as the directed path element along C_1. Now, $B_z = 0$ outside of the time-dependent neighborhood $S_r(t)$ where the relaxing flux-rope is reconnecting with the untwisted fields. Let F_0 be the total axial flux across $S_r(t)$. Then, we have

$$\frac{dF_0}{dt} = \oint_{C_1} (\mathbf{v} \times \mathbf{B} - \eta \nabla \times \mathbf{B}) \cdot d\mathbf{s}, \tag{52}$$

where C_1 is any curve large enough to include $S_r(t)$. Take C_1 to run along $y = 0$ and close at infinity in $y > 0$. No disturbance can reach infinity in $y > 0$ so that we may set $\mathbf{v} = 0$ in the far reaches of the domain, in addition to neglecting η. We also have boundary condition (50) and a negligible η at $y = 0$. Therefore, within these approximations, the total axial flux F_0 is a constant in time.

4.4. Energy Comparison

The basic formulation of the Taylor theory for the open atmosphere $y > 0$ is now complete. Our model poses the following interesting problem in variational calculus, generalizing from the minimum-energy theorem of Woltjer (1958). Subject to boundary conditions (15) and (16) and the contraints of given total helicity H_R and total axial flux F_0, ask for a state of extremum total magnetic energy. We take the total magnetic energy to be renormalized to be the energy in excess of that in the everywhere potential field $\mathbf{B}_{min}$ satisfying boundary condition (15), in order to avoid dealing with unbounded total energies.

Without any further qualification, this variational problem taken in the Woltjer sense would require the finite total helicity H_R and total axial flux F_0 to spread throughout the domain $y > 0$. This corresponds to the possibility we have dismissed, that is, the helicity and axial-flux density would tend to zero, and the minimum-energy end state would in this case be $\mathbf{B}_{min}$.

On the other hand, if the spread of total helicity and axial flux is halted at some flux surface $\partial\sigma$, then $\mathbf{B}$ must have a minimum energy in σ as well as σ' treated as two separate regions, subject to the fixed values in H_R and F_0. Since the helicity and flux are both zero in σ', the minimum-energy field in σ' is potential subject to boundary conditions (15) and (16) and the requirement that $\partial\sigma$ is a flux surface.

The problem for the minimum-energy state in σ then takes the form

$$\delta \int_\sigma \left(|\nabla A|^2 + Q^2 \right) dx dy = 0, \tag{53}$$

subject to the constraints of fixed values of H_R and F_0. Since $\partial\sigma$ is a flux surface $A = A_0$, this variational problem is subject to the boundary condition

$$\delta A|_{\partial\sigma} = 0. \tag{54}$$

Introducing Lagrangian multipliers Λ_1 and Λ_2, this variational problem is equivalent to

$$\delta \int_\sigma \left(|\nabla A|^2 + Q^2 + \Lambda_1 A Q + \Lambda_2 Q \right) dx dy = 0, \tag{55}$$

subject to boundary condition (54). The Euler-Lagrangian equations for this problem are

$$2Q + \Lambda_1 A + \Lambda_2 = 0, \tag{56}$$
$$\nabla^2 A - \Lambda_1 Q = 0, \tag{57}$$

requiring $Q(x, y)$ to vary in space as a linear function of $A(x, y)$. We recover the linear partial differential equation (7) for a constant $\alpha_0 = \frac{1}{\sqrt{2}}\Lambda_1$ force-free field. The constant Lagrangian multipliers are determined by imposing on the solution to have the specific values of H_R and F_0 given.

In the above treatment of the variational problem, we are assuming a fixed domain σ such that $A = A_0$ on $\partial\sigma$, where A_0 is known and the solutions in σ and σ' describe a continuous $\mathbf{B}$ across $\partial\sigma$, essentially *assuming* that the free-boundary problem treated in Section 3 exists. We have not proven mathematically that the solution exists. The numerical solutions by direct construction is the basis for assuming that the solution exists. We also cannot rule out by our variational consideration that for a fixed pair (H_R, F_0), more than

one solution $\mathbf{B}$ may exist but with different σ-σ' partition of the domain. If there are more than one solution, then the one with the lowest energy will be the preferred final state of the field relaxation.

A more general theory of extremization to exhaust all possibilities of the (σ, σ') is formidable, but our numerical solutions of Section 3 suggest that for each prescribed pair of (H_R, F_0), the pair of (σ, σ') found as a free-boundary solution is unique, at least, for the parametric regime covered by our numerical study. In principle, our iterative procedure could lead to convergence to other pairs of (σ, σ') with the same (H_R, F_0), but none were encountered.

Our extremization suggests that the constant axial-current, flux-rope solutions is at a higher energy state than the corresponding one with a constant α having the same (H_R, F_0). This indication is borne out by our numerical study in that every pair of comparison fields with the same (H_R, F_0) show that the constant-α field is of the lower total magnetic energy. Each pair of fields thus represent a Taylor relaxation from a higher-energy state to a minimum-energy state through a re-distribution of both H_R and F_0.

The very small energy change, less than 2% in each case, was unanticipated. We had set out in the study to find any pair of initial-final states in order to carry out an energy comparison. The final state is, of course, to be the minimum energy state, namely, a constant-α field, in which case any non-constant α field would serve as a higher energy state. In that consideration, we simply chose the uniform axial-current fields because their governing equation is reducible to a linear partial differential equation. We have discovered by direct numerical construction that these uniform axial-current fields are energetically close to the absolute minimum. Hu (1999) has shown that all the cylindrically symmetric fields of this class are ideally stable to linear perturbation, so that our result is perhaps not surprising.

The energy of a force-free flux rope depends on how the field is spatially distributed. The third example of a cylindrically symmetric rope given by equations (35) and (36) illustrate the point. Table 1 shows the energy E_i of this rope as a function of rope radius R_1 to be compared with the energy E_c of the constant-α field sharing the same F_0 and H_R. For the broad range of rope radius in the table, the energy change is large, of the order of $40-60\%$, in sharp contrast to the case of the constant axial-current fields. Taylor relaxation is a process of reconnection to distribute a given amount of flux and twist in a rope evenly subject to the conservation of these two quantities.

R_1		E_i		E_c		% decrease
0.3		41.2583		16.6103		60%
0.4		32.5567		14.8033		54%
0.5		27.2910		13.4016		51%
0.6		23.6769		12.2562		48%
0.7		20.9506		11.2880		46%
0.8		18.7309		10.4494		44%

Table 1: The initial energy, E_i, the constant alpha solution, E_c, % decrease for various R_1

4.5. Flux-Rope Implosion

Note that the A-values defining the flux surfaces of constant-A intersecting the boundary $y = 0$ are fixed during the relaxation, under boundary condition (15). Since $A < 0$ on that boundary, the closed fields lying entirely in $y > 0$ and circulating around the flux rope have positive A values. These closed fields indicate by Ampere's law the presence of the axial current of the flux rope. Denote the flux function values on $\partial \sigma$ to be A_1 and A_2, respectively, before and after relaxation. It follows from these properties that the advance of $\partial \sigma$ into the initially untwisted external fields as a result of relaxation implies that $A_1 > A_2$. This inequality is satisfied for all the pairs of initial-final states found in our numerical study. Figures 6 and 7 show two particular cases.

The inequality $A_1 > A_2$ is associated with a hydromagnetic implosion first pointed out by Hudson (2002). The magnetic energy density $\frac{B^2}{8\pi}$ is also the magnetic pressure. Therefore, a significant loss of magnetic energy in a volume V implies a reduction of the average magnetic pressure in that volume. If V does not change, say, in the case of a magnetic field contained in a rigid container, this reduction of magnetic pressure has the unremarkable effect of a reduction of that pressure exerted on the rigid container wall; see the example of Zhang & Low (2003). On the other hand, the liberation of magnetic energy has a remarkable observable consequence if it takes place within a flux system naturally surounded by other flux systems in an atmosphere; see the examples in Janse & Low (2007). As a result of the loss of mean magnetic pressure in that flux system, it would contract as the surrounding flux systems expand by their superior magnetic pressures. This effect, inherent in Taylor relaxation taking place in an open atmosphere, is in full evidence in our numerical solutions.

In each pair of initial-final states, in addition to the inequality $A_1 > A_2$, the following features are also found. First note that $A = A_2$ in the initial state lies outside of the flux-rope boundary $\partial \sigma$ where $A = A_1$. The untwisted external flux sandwiched between these two

flux surfaces becomes a part of the flux rope in the final state, which explains why $A = A_2$ on $\partial\sigma$ in the final state. Another way of looking at this transition is to say that the energy liberation has taken place within the flux surface $A = A_2$ as this surface evolves from its initial location to its final location in the two states. The flux within $A > A_2$, including the flux rope, has lost energy and has also weakened its mean magnetic pressure. We therefore expect in this transition, the potential field external to $A = A_2$ to expand and compress the energy liberating region. That is, the curve $A = A_2$ in the initial state must contain, as whole, the curve $A = A_2$ corresponding to $\partial\sigma$ in the final state. This is found to be the case for all field relaxations in our numerical solutions . As shown by the explicit examples in Figure 9, the curve $A = A_2$ contracts inward in that transition with the possibility of zero contraction at a common point at the bottom of the two curves.

4.6.   The Influence of the Lower Boundary

The above change in the internal rope structure can be understood in relation to the global force-balance that determines the location of the flux rope before and after relaxation. The inductive response of the perfectly conducting boundary $y = 0$ has a central role.

By definition, in a force-free field, the net force exerted by all the other currents in the system on any piece of local current is zero. There are two aspects to this property: the one relating to the shape and internal equilibrium of the flux rope and the other relating to the flux-rope location. Consider a flux rope of a small cross-sectional area σ. Then the two aspects may be approximately separated (Forbes 1990).

Decompose the equilibrium field $\mathbf{B}$ in $y > 0$ linearly as

$$\mathbf{B} = \mathbf{B}_{min} + \mathbf{B}_{rope}, \tag{58}$$

where $\mathbf{B}_{rope}$ is, by definition, the excess field above the everywhere potential field $\mathbf{B}_{min}$ uniquely defined by boundary conditions (15) and (16). The field $\mathbf{B}_{min}$ can be attributed to a virtual line current of some intensity $I_0 = \frac{1}{2}cB_0$ flowing in the z-direction located at $(x, y) = (0, -1)$. By definition, $\mathbf{B}_{rope}$ satisfies the boundary condition

$$\mathbf{B}_{rope} \cdot \mathbf{n} = 0 \; at \; y = 0, \tag{59}$$

where $\mathbf{n}$ denotes the unit outward normal vector at the boundary. This boundary condition implies that $\mathbf{B}_{rope}$ must be generated by the flux-rope current-density $\mathbf{J}$ in $y > 0$ combined with a virtual, image current system $\mathbf{J}_I$ located in $y < 0$.

Denote by I_{rope} the net axial current in the rope. Then the net axial current in the $\mathbf{J}_I$ system is $-I_{rope}$. For the field configurations in Figures 6 and 7, I_{rope} and I_0 are both

positive by the right hand rule. Therefore, the force-free state of the rope is achieved by a balance of two two Biot-Savat forces, one that is repulsive between the two opposite currents $\pm I_{rope}$ and the other attractive between the rope current I_{rope} and the like-sign current I_0 of the background field. Suppose the thin flux rope is located at height $y = y_0 > 0$. Then, by the Biot-Savat formula for the force between 2 line currents, the above force balance is expressed by

$$\frac{I_{rope}^2}{2y_0} = \frac{I_{rope}I_0}{y_0 + 1}. \tag{60}$$

The rope location is given in terms of the net current I_{rope} by

$$y_0 = \frac{I_{rope}}{2I_0 - I_{rope}}. \tag{61}$$

Several implications can be made. The current I_0 is fixed by the boundary flux at $y = 0$. For a rope in $y > 0$, we require $2I_0 > I_{rope}$ putting a limit on the net current in the rope. For I_{rope} too close to or in excess of this limit, the assumption of a thin flux rope would have broken down. There is also the possibility that for larger values of I_{rope}, the rope is no longer entirely confined within the domain $y > 0$. Conceivably reconnection can spread so far out into the potential field as to pass helicity and axial flux into the part of the external flux that are connected to $y = 0$. In this case, the conservation of the axial flux discussed in Section 4.3 needs to be re-examined. These considerations lie outside the scope of the present study that is defined by the numerical methods we have developed.

Assuming the thin flux rope approximation within the limit $2I_0 > I_{rope}$, it is clear that the larger I_{rope} is, the higher the rope is located in the domain. This is the basic effect underlying the parametric trends found in our numerical solutions, that the height of the flux rope increases with independent increases of F_0 and H_R. An increase of axial flux or helicity corresponds generally to an increase of the axial current. A Taylor-like relaxation reduces the free energy of the system and that manifest in a decrease of the presence of current, subject, of course, to the conservations laws. Hence, the flux rope following a relaxation and the reduction of current tends to be relocated lower in height as found in the pairs of initial-final states of our numerical study.

5. Summary and Conclusion

Our numerical study applies the Taylor theory to field relaxation in an open atmosphere, based on a two-dimensional model. The free-boundary solutions posed for a flux rope relaxing in an interacting external potential field illustrate the topological changes produced by reconnection. The theory extension dealt with two complications. The first is

not new, namely, the need to use the relative total helicity of Berger & Field (1984). The other arises from the resistive reconnection between the rope and its surrounding flux with physical effects basic to the creation of long-lived structures in the solar corona. The effects discussed in our analysis have been encountered in various forms in coronal modeling but a self-consistent demonstration of how they work together had not been possible. This is because the governing equations of force-free fields, even for a geometrically simplifying two-dimensional model, are nonlinear.

With no wall to confine a relaxing flux rope, the region of reconnection spreads outward from the initial flux rope and the question arises whether this spreading would stop. Our solutions show that the reconnection can, indeed, stop at some outer flux surface within which the reconnected field attains a minimum-energy, constant-α force-free state of Woltjer (1958). The energy available for reconnection is constrained by the conservation of total axial flux and helicity. That energy simply has run out when this final state of minimum energy is reached. This result provides motivation to numerically simulate the time-dependent Taylor process using the full set of hydromagnetic equations. The point here is that a postulated transition consistent with the relevant conservation laws is only a necessary but not sufficient condition for its reality.

It should also be pointed out that our numerical study has not exhausted all topological possibilities for a pair of initial-final states in the two-dimensional model. Notably, we have not explored the possibility of the reconnection spreading to reach the base of the atmosphere. There is a natural extension of our model to realistic geometry, the one involving a rope of twisted magnetic field that is anchored at both ends to the coronal base, embedded in an external global potential field. This three-dimensional model will bring the physical effects treated in this paper an important step towards the realistic magnetic topologies of coronal observations.

Our numerical solutions illustrate cleanly the interesting physical effect of hydromagnetic implosion associated with magnetic-energy release pointed by Hudson (2002) and treated less completely in some recent studies (Zhang & Low 2003, Janse & Low 2007). The outward migration of the magnetic boundary of a reconnecting flux rope is complicated by the compression of the relaxing field as it loses its internal magnetic pressure. This effect probably operates on all physical scales. It would be interesting to look for its signature in coronal observations.

REFERENCES

Alexander, D., & T. R. Metcalf 2003, Solar Phys. 210, 323

Aly, J. J. 1989, Solar Phys.120, 19

Aly, J. J., & T. Amari 2007, GAFD 101, 249

Amari, T., & J. F. Luciani 2000, PRL 84, 1196

Amari, T., J. F. Luciani, J. J. Aly, Z. Mikic, & J. Linker 2003, ApJ 585, 1073

Amari, T., J. F. Luciani, & J. J. Aly 2004, ApJ 615, 165
        Aly, J. J., & T. Amari 2007, GAFD 101, 249

Aschwanden, M. 2005, *Physics of the Solar Corona*, Springer

Berger, M. A. 1985, ApJ Suppl. 59, 433

Berger, M. A 1984, Geophys. Astrophys. Fluid Dyn. 30, 79

Biskamp, D. 2000, *Magnetic reconnection in plasmas*, Cambridge U. Press, Cambridge.

DA moulin, P. 2007, Ad. Sp. R.39, 1674

Demoulin, P., E. Pariat, M. A. Berger 2006, Sol. Phys. 233, 3

Dixon, A. M., M. A. Berger, E. R. Priest, & P. K. Browning 1989, AA, 225,156

Elcrat, A., Fornberg, B., Horn, M. & Miller, K. 2000, J. Fluid Mech. 409, 13

Elcrat, A., Fornberg, B. & Miller, K. 2001 J. Fluid Mech. 433, 315.

Fan, Y. 2001, ApJ 554, L111

Fan, Y., & S. E. Gibson 2004, ApJ 609, 1123

Flyer, N., B. Fornberg, S. Thomas, & B. C. Low 2004, ApJ 606, 121

Forbes, T. G. 1990, JGR 95, 11919

Forbes, T. G., & E. R. Priest 1995, ApJ 446, 377

Gibson, S. E., et al. 2002, ApJ 574, 265

Heyvaerts, J., & E. R. Priest 1984, A & A A 137, 63

Hu, Y. Q. 1999, Acta Astron. Sin. 40, 394

Hu, Y. Q. & Zh. Wang 2005, ApJ 623, 551

H. Hudson, Astrophys. J 531, L75

Janse, A. M., & B. C. Low 2007, AA 472, 957

Kulsrud, R. M. 1998, Phys. Plasmas 5, 1599

Krucker, S., & R. P. Lin 2003, Solar Phys. 210, 229

Lin, R., B. R. Dennis & A. O. Benz (Eds) 2003, *The Reuven Ramaty High-Energy Solar Spectroscopic Imager (RHESSI)-Mission description and early results*, Kluwer Academic Publisher, Dordrecht

Lites, B. W., 2005, ApJ 622, 1275

Lites, B. W., et al. 1995, ApJ 446, 877

Low, B. C. 1996, Sol. Phys. 167, 217

Low, B. C. 2006, ApJ 649, 1064

Low, B. C. 2007, Phys. Plasma 12, 122904

Low, B. C., & M. A. Berger 2003, ApJ 589, 644

Low, B. C., & N. Flyer 2007, ApJ 688, 557

Low, B. C., & Y. Q. Lou 1992, ApJ 352, 343

Magara, T. 2006, ApJ 653, 1499

Magara, T., S. Mineshige, T. Yokoyama, & K. Shibata 1996, ApJ 466, 1054

Manchester, IV, W. 2001, ApJ 547, 503

Manchester, IV, W., et al. 2004, ApJ 610, 588

Okamoto, T. J., et al. 2007, ApJ 673, L215

Parker, E. N. 1979, *Cosmical Magnetic Fields*, Oxford University Press

Parker, E. N. 1994, *Spontaneous Current Sheets in Magnetic Fields*, Oxford University Press

Roberts, P. H. 1967, *An Introduction to Magnetohydrodynamics*, American Elsevier

Sakurai, T. 1989, Space Sci. Rv. 51, 117

Shibata, K., S. Nozawa, S. Matsumoto, A. C. Sterling, & T. Tajima 1990, ApJ 351, L25

Shibata, K., S. Masuda, M. Shimojo, H. Hara, T. Yokoyama, S. Tsuneta, T. Kosugi & Y. Ogawara 1995, ApJ 451, L83

Shibata, K. 1999, Astrophs. Sp. Sci. 264, 129

Spitzer, L. 1965, *Physics of fully inonized gas*, Interscience, New York

Taylor,J. B. 1974, Phys. Rev. Lett. 33, 1139

Taylor,J. B. 1986, Rev. Mod. Phys. 58, 741

Titov & Demoulin 1999, A & A 351, 707

Tsuneta, S. 1996a, ApJ 456, 840

Tsuneta, S. 1996b, ApJ 464, 1055

Wolfson, R., 2003, ApJ 593, 1208

Wolfson, R., J. Larson & R. Lionello 2007, ApJ 660, 1683

Woltjer, L. 1958, Proc. Nat. Acad. Sci. USA 44, 489

Yamada, M. 2001, Earth, Planet & Space 53, 509

Zhang, M., 2006, ApJ 646,85

Zhang, M., & B. C. Low 2003, ApJ 584, 479

Zhang, M., & B. C. Low 2005, ARAA 43, 103

Zhang, M., N. Flyer & B. C. Low 2006, ApJ 644, 575